International Journal of Mass Spectrometry 278 (2008) 75–88

Contents lists available at ScienceDirect

International Journal of Mass Spectrometry

journal homepage: www.elsevier.com/locate/ijms

Comparison of quadrupole mass filters equipped with rods of different convexity: An analysis by finite element methods and trajectory simulations

Gianangelo Bracco*

CNR-IMEM and Physics Department, University of Genoa, via Dodecaneso 33, I-16146 Genoa, Italy

ARTICLE INFO

Article history:
Received 31 October 2007
Received in revised form 21 August 2008
Accepted 22 August 2008
Available online 2 September 2008

Keywords:
Quadrupole mass filter
Laplace equation
Finite element method
Ion trajectory simulation

ABSTRACT

A quadrupole mass filter is generally built by using cylindrical rods whose radius and separation are chosen to approximate the ideal hyperbolic field. Recently, concave cylindrical as well as planar geometries have been proposed to replace ordinary cylindrical rods with the aim to reduce the size and weight of the filter. In this article, the geometry of four configurations (convex, modified convex, planar, and concave) is investigated by means of calculations based on finite element methods which provide an accurate modeling of the geometry. For each configuration the optimized geometry which approximates at best the ideal hyperbolic field is determined. In the literature, results on the convex configuration showed that the optimized geometry does not lead to the best values for mass resolution and transmission, therefore, in this study, other geometries around the optimized ones have been investigated. The transmission has been estimated by performing trajectory simulations for ions injected in the field generated by each studied geometry. The comparison among the different rod configurations shows that convex rods work better than concave and planar ones. Therefore, the proper choice for compact and light mass filters is the modified convex geometry.

1. Introduction

Mass spectrometers are widely used in a variety of fields to separate different atomic or molecular species. They exploit the difference in mass-to-charge ratio (m/e) to transmit only one of the selected species. The selection is often made by a quadrupole mass filter developed in the 1950s by Paul et al. [1–3] which consists of four parallel metal rods arranged symmetrically on a circle as shown in Fig. 1a. Opposite rods are electrically connected and a dc voltage (U) plus an ac voltage ($V\cos(\omega t)$, $\omega = 2\pi f$, f the frequency of the ac voltage) are applied to the two pairs. The applied voltages determine a field between the rods which affects the trajectory of ions traveling along the filter. For selected dc and ac voltages, only ions of a specific mass-to-charge ratio are allowed to pass through the quadrupole filter with high probability and all other ions are in some way rejected.

Ideally, the field should be a quadrupolar hyperbolic field produced by four parallel rods of hyperbolic cross section [1,4]. Assuming that the charged particles are injected in the field with velocity $\underline{v}$, as schematically shown in Fig. 1b, the particles feel the variable field $\Phi = [U + V\cos(\omega t)]((x/r_0)^2 - (y/r_0)^2)$ where r_0 is the field radius, i.e., the distance between the axis and the nearest point on the rod ($2r_0$ is the diameter of the free space between the rods). Hence, the particles are not accelerated along z, i.e., $v\cos(\chi)$ is constant, while perform oscillatory trajectories in the perpendicular x and y directions which are described along the two axes by equations of the type

$$\frac{d^2u}{d\tau^2} + (a - 2q\cos(2\tau))u = 0, \quad (1)$$

i.e., the Mathieu equation [5], with u representing x or y,

$$a = \frac{8eU}{m\omega^2 r_0^2} = a_x = -a_y,$$
$$q = \frac{4eV}{m\omega^2 r_0^2} = q_x = -q_y,$$

and $\tau = \omega t/2$, t is the time. As well known, the solutions to Eq. (1) are of two types: stable, where the oscillation amplitude remains finite, and unstable, where the amplitude diverges with time. Of course, particles must have a stable trajectory along both the x and y directions. The sets of values of a and q where the stability conditions are met determine the stability regions in the (q, a) plane and the first stability region, close to the origin, has a quasi-triangular shape with the vertex at $q = 0.706$ and $a = 0.23699$ [6].

* Tel.: +39 010 3536287; fax: +39 010 3622790.
E-mail address: bracco@fisica.unige.it.

1387-3806/$ – see front matter © 2008 Elsevier B.V. All rights reserved.
doi:10.1016/j.ijms.2008.08.016

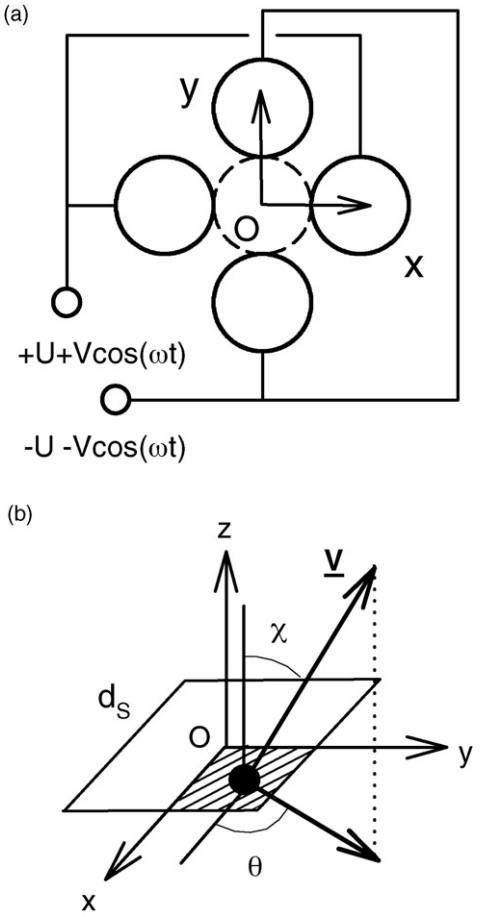

Fig. 1. (a) Schematic cross section of a quadrupole mass filter. The four circles (solid lines) represent the rods. The dashed circle represents the region of radius r_0. The rods are connected in pairs and an ac voltage at angular frequency ω plus a dc component are applied to the two pairs. The reference system xy used in the field calculations is also shown. (b) Reference system used in the trajectory calculations: $\underline{\mathbf{v}}$ is the ion velocity, χ is the polar angle between the velocity and the z axis, θ is the azimuthal angle between the velocity projection on the xy plane and the x axis. The shaded region in the first quadrant is the injection area employed in the simulations of the full squared injection region with edge $d_S \leq r_0$.

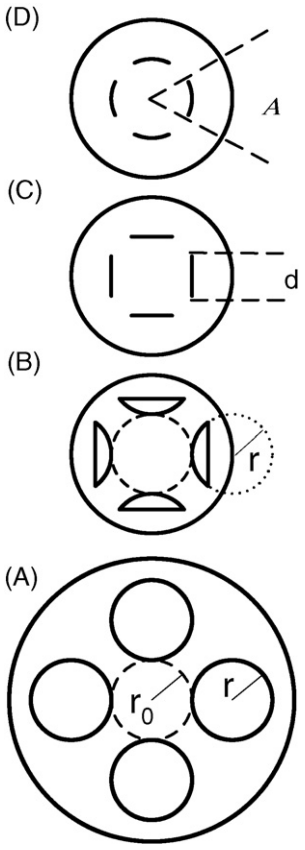

Fig. 2. Comparison between the cross sections corresponding to different rod configurations which have the same radius r_0 of the free space between the rods (dashed circle). The convex configuration (A) is the ordinary geometry used in quadrupole mass filters (ORs). The modified ordinary rods (MRs) (B), where only a fraction of the full rod (dotted line) is used, the planar rod configuration (PRs) (C) and the concave rod configuration (CRs) (D) are lighter and smaller than A. Parameters used in the calculation are the rod radius r (A, B), the rod width d (C), and the rod angular extension A (D).

Hyperbolic rods can be machined [7] but their alignment is difficult; therefore, cylindrical rods are generally used in commercial devices [8,3]. The field generated by cylindrical rods, which depends on the rod radius r, should approximate the hyperbolic field at least in a region around the quadrupole axis. A first empirical investigation to optimize the geometry was conducted by Dayton et al. [8]. They measured a ratio $r/r_0 = 1.148$, where r_0 has the same meaning as for hyperbolic rods, for obtaining the best approximation to the hyperbolic field. Later, a calculated value of r/r_0 was obtained numerically by Denison [9] in the case of four cylindrical rods inside a cylindrical housing. He showed that the best approximation is obtained by using a ratio $r/r_0 = 1.1468$. More recent analytical calculations performed by Reuben et al. [10,11] and based on conformal mapping found a slightly different value $r/r_0 = 1.14511$. Thus, the diameter of the field is less than the diameter of the rods and the space in the mass filter is almost entirely filled by the rods. This has a negative effect on the weight of the device and also on its capacitance which appears in the relationship of the power needed to drive the filter. Instead for applications such as space-based missions the possibility to reduce the weight and the power consumption are of primary importance. Apart attempts based on microelectromechanical systems (MEMS) [12,13] which solve only the problem of a reduced size of the filter, a more efficient use of the internal space is solved by changing the geometry of the rods and cylindrical concave rods have been recently constructed as an alternative to conventional cylindrical rods [14]. In Fig. 2, this rod type is shown and compared to conventional rods. It is clear the advantage of a smaller size which in turn means a reduction in weight and capacitance. Moreover, also the planar (rectangular) geometry has been constructed using techniques employed to manipulate semiconductor such as the molecular beam epitaxy [15]. The planar rods present similar reduction in size and weight and are also shown in Fig. 2.

Investigations on both these unconventional geometries actually started at the end of the 1960s with the work by Sakudo and Hayashi [16–18]. They calculated the optimized geometries and verified experimentally the analitical results with the field plotting method. They found that the optimized angular extension for the concave cylindrical rods is $A = 37^\circ$ (infinite rod thickness) or 44° (infinitesimal rod thickness) and that the optimized length for planar rods is $d = 0.672r_0$ (trapezoidal rods) or $0.818r_0$ (rectangular rods) of infinite thickness.

In this article the change from convex geometry, which is more similar to the hyperbolic case, to planar and concave ones is investigated since this change should affect the mass selection and the stability conditions on ion trajectories. Moreover, a fourth geometry is also included. In fact, in the design of detectors for He scattering apparatuses [19,20] employed for investigating supersonic

beam properties [21,22] and structural properties of crystalline surfaces [23,24], my group has tackled the problem of weight and size reduction of a conventional mass filter and I started to numerically investigate cylindrical modified rods by means of finite element methods. Modified rods are convex cylindrical rods whose full cross section with radius r is reduced, as shown in Fig. 2, and the convexity is preserved. For this article, the rod thickness is kept constant at $0.4r_0$ to maintain the same size of the housing used for planar and concave rods. The analysis, therefore, has been performed on the four rod configurations of Fig. 2.

The first part of the analysis has been devoted to calculate the geometry which provides a field closer to the hyperbolic one, both with the Denison method and with a novel procedure. In the second part, ion trajectory simulations has been carried out to estimate the ion transmission through a mass filter in order to evaluate the performance also in the case of unconventional (non-convex) rods. Results published in literature have shown that perturbations to the hyperbolic field is beneficial to transmission and resolution of the filter. In particular, the effect of the first two perturbing multipolar terms of Eq. (2), i.e., the terms with $n = 1, 2$, and the possibility to work with increased $n = 1$ or $n = 2$ terms have been investigated in the case of cylindrical convex rods [25–27]. One of the findings is that the best performance of the filter is for $r/r_0 \simeq 1.130$. Also Gibson and Taylor [28] investigated the change in r/r_0 for cylindrical convex rods and found better performance in the range between 1.120 and 1.130. Therefore, those results prove that the best approximation to the hyperbolic field alone does not guarantee also the best performance of the filter. Thus the simulations of the present article have been carried out as a function of the parameters which describe the four geometries for a suitable range around the calculated values determined in the first part. In this way the parameters for the best performance will be determined for the four configurations and finally their performances will be compared.

2. Quadrupolar field calculations

The potential field ϕ inside an infinite quadrupolar structure ignoring space charge effects is the solution of the Laplace equation $\nabla^2\phi = 0$. Assuming a cartesian orthogonal system with the origin on the quadrupole axis and with the x and y axes passing through the centers of the rods (see Fig. 1a), the field can be expressed by a series of multipolar terms as

$$\phi = (U + V\cos(2\pi f))\sum_k B_k(\rho/r_0)^k \cos(k\theta)$$

where $\rho = \sqrt{x^2 + y^2}$ and $\tan(\theta) = y/x$ are the polar coordinate inside the region r_0.

Moreover, the arrangement of the 4 rods requires that field must change sign when θ is changed by $\pi/2$, i.e., $\cos(k\pi/2) = -1$. This symmetry requirement imposes restriction on the possible k values and the allowed ones are $k = (2(2n + 1))$ with n a non-negative integer. Therefore, the field with the appropriate symmetry is

$$\phi = (U + V\cos(2\pi f))\sum_n B_n\left(\frac{\rho}{r_0}\right)^{(2(2n+1))} \cos(2(2n + 1)\theta). \quad (2)$$

The ideal quadrupole field is given by the $n = 0$ term, instead the other higher order multipole terms

$$P = \sum_{n>0} B_n(\rho/r_0)^{(2(2n+1))} \cos(2(2n + 1)\theta) \quad (3)$$

act as a perturbation to the ideal case.

This perturbation affects the ion motion in the filter as can be easily checked by differentiating Eq. (2) and the equations of motion are expressed by

$$\frac{d^2x}{d\tau^2} = -(a + 2q\cos(2\tau))\sum_n (2n + 1)B_n\left(\frac{x^2 + y^2}{r_0^2}\right)^{(2n)} \times [x\cos(2(2n + 1)\theta) + y\sin(2(2n + 1)\theta)]$$

$$\frac{d^2y}{d\tau^2} = -(a + 2q\cos(2\tau))\sum_n (2n + 1)B_n\left(\frac{x^2 + y^2}{r_0^2}\right)^{(2n)} \times [y\cos(2(2n + 1)\theta) - x\sin(2(2n + 1)\theta)]$$

where a and q are the usual parameters introduced in Eq. (1). The equations with only the $n = 0$ term ($B_0 = 1$, $B_n = 0$) are of course related to the Mathieu equation and separately depend on x or y; therefore, the ion motion evolves independently on the two axes. Instead the higher order multipole terms couple the motions along the two axes and may modify the stability condition. In order to establish the extent of the perturbation of high order multipole terms, the potential ϕ has been calculated by using a finite element approach. Finite element methods divide the problem of interest into a mesh of geometric shapes called finite elements. The potential within an element is described by a function that depends on its values at the element vertices. The code related to the finite element method was written in MATLAB following Ref. [29] and adapting it to the present geometry. The developed software automatically generates the net of points that are used to divide the calculation region in triangles. The starting mesh is a uniform distribution of points. Then the mesh is optimized following a procedure described in Ref. [30] which has been suitably modified for the present calculation. The algorithm ensures that the boundaries are always well described hence the solution accurately satisfies the boundary conditions. In each calculation the rods are surrounded by a cylindrical case of radius R having a potential $\phi = 0$. To increase the accuracy of the calculations, only half of one quadrant between electrodes has been considered (see Fig. 3) since the other parts can be obtained by exploiting the symmetry of the problem, i.e., $\phi(y, x) = -\phi(x, y)$, $\phi(-x, y) = \phi(x, y)$, and $\phi(x, -y) = \phi(x, y)$. Therefore, on the $x = y$ segment the potential ϕ vanishes while along the non-negative x axis, apart the crossing of the rod, its normal derivative is zero. The potential of the rod has been set to $\phi = 1$.

The accuracy of the method has been tested for a cylindrical geometry (cylindrical capacitor) where analytical results are easily calculated. The relative difference between numerical and analytical calculations does not exceed 10^{-7} for a density of points similar to that used in the calculation of ϕ.

As shown in Fig. 2, the free space between opposite rods has radius r_0, while the parameter which is varied depends on the configuration. For ordinary cylindrical rods (ORs) or modified rods

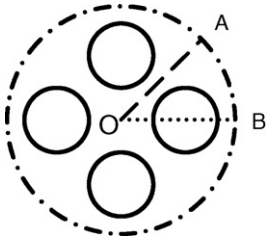

Fig. 3. Circular sector OAB where the potential ϕ has been calculated: it is delimited by the $x = y$ segment (dashed line OA), the non-negative x axis (dotted line OB) and the housing (dash-dotted line). The potential ϕ vanishes on $x = y$ and its normal derivative is zero on the x axis, excluding the crossing of the rod. The potential is set to $\phi = 1$ on the rod while is zero on the housing. The example shows the case for cylindrical rods but a similar scheme has been adopted for all the rod configurations.

(MRs), it is the rod radius r; for planar rods (PRs) it is the width d of the rods; for concave cylindrical rods (CRs) is the opening angle A of the rods. For PRs and CRs the thickness of the rods is fixed at $0.2r_0$. The housing has radius $R = 2r_0$ for MRs, PRs, and CRs while $R = 3.54r_0$ for ORs. After the calculation of ϕ, a fitting procedure is carried out to determine the coefficients B_n of the series in Eq. (2). The selected points are those which lie within the field radius r_0. Their exact number depends on the configuration: about 2.3×10^4 for ORs, more than 4.7×10^4 for MRs, and about 3.3×10^4 for PRs and CRs. A test has also been performed for hyperbolic rods of finite extent enclosed in a case with $R = 5.5r_0$ and the fitting procedure has shown that ϕ is represented by a series with $B_0 = 1$ and $|B_n| < 10^{-6}$, $n > 0$, close to what expected for an ideal hyperbolic field.

For ORs, Denison [9] and other authors [11,16–18] searched for the vanishing of B_1 (this procedure will be referred to as VB_1) to determine the optimized geometry. This is almost correct for ORs and MRs because the B_n's rapidly tends to zero with n but, where B_1 is zero, the next higher order term obviously assumes an important role [31]. Instead for the unconventional rods, PRs and CRs, higher order terms have a value similar to B_1 and the convergence of the multipolar series is very slow due to the different convexity close to the rods with respect to the hyperbolic field. Therefore, the vanishing of B_1 is not the correct way to search for the optimized geometry and the search for a minimum of the global perturbation P seems the appropriate way. I have considered the squared norm of P, $N_2 = \|P\|^2$, which can be calculated, taking into account that cosine functions with different n are orthogonal, as the sum of the squared terms of Eq. (3) integrated on the circle of radius r_0. The parameter value which allows the minimization of N_2 (this procedure will be referred to as MN_2) provides the optimized geometry. The number n of terms has been chosen to reproduce the field with good accuracy. With $n \leq 15$, the maximum difference between the calculated ϕ and the truncated series is less than 1.5×10^{-6} for ORs, 1.2×10^{-6} for MRs, 3×10^{-5} for PRs. Instead for CRs, n has been increased to 50 obtaining a maximum difference $< 10^{-4}$ within a region corresponding to 99% of the field radius r_0. In particular, the maximum discrepancy for CRs is about 4.6×10^{-3} only for a few points located close to the edge of the rod where the field is expected to differ most from the hyperbolic one.

In Fig. 4, N_2 and B_1 are plotted vs. the parameters of the geometries. In the case of ORs, the VB_1 method provides a value which agrees with recent determinations [11,31] and very close to that calculated with the MN_2 method as shown in Table 1. Moreover, the calculated values of B_n differ by less than 10^{-3} with those reported in Ref. [11]. For PRs and CRs, the perturbation and B_1 values are greater than those of ORs, as observed above. The VB_1 values are consistent with those calculated in Refs. [16–18] taking into account that in the present case the rod thickness is finite and the rods are surrounded by an housing. Moreover, the MN_2 and VB_1 methods provide different results although the N_2 curves present a broader minimum with respect to that of ORs. In order to quantify this broadening, the minimum value Y_m of each N_2 curve has been increased of 1%, the intersection of the appropriate constant $1.01Y_m$ with the curve gives rise to a semi-interval around the minimum which is $\Delta d/r_0 = 0.0116$ for PRs, $\Delta A = 0.6°$ for CRs, $\Delta r/r_0 = 0.0030$ for MRs, and $\Delta r/r_0 = 0.0029$ for ORs. This confirms that within a 1% variation of the minimum, the VB_1 method provides the same result as the MN_2 one for ORs and MRs, while, for unconventional rods, the two methods yield different results.

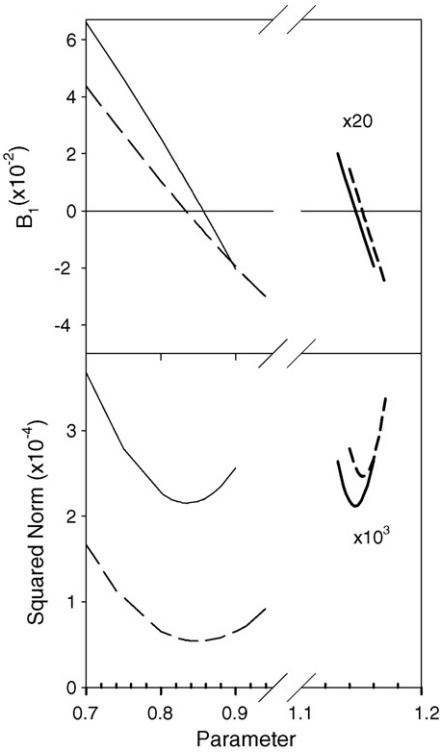

Fig. 4. Results of the calculations performed on the different rod configurations. In the upper panel the coefficient B_1 is shown while the squared norm of the perturbation P is displayed in the lower panel. Convex configurations (ORs and MRs) are depicted on the right part. Solid (dashed) curves are related to ORs and CRs (MRs and PRs). For ORs and MRs, the curves have been multiplied by a factor 20 and 10^3, respectively. For CRs, the parameter $A/45°$ is shown.

Table 1
Parameters which provide the optimized geometry using the minimum of the perturbation N_2 (MN_2) or the vanishing of B_1 (VB_1)

Geometry	Parameter	MN_2	VB_1	B_0
ORs	r/r_0	1.1449	1.1451	1.0028
MRs	r/r_0	1.1510	1.15067	1.0029
PRs	d/r_0	0.8484	0.8332	1.036
CRs	A ($A/45°$)	37.59° (0.83542)	38.55° (0.85656)	1.060

The last column reports the coefficient B_0 of Eq. (2) estimated for MN_2.

3. Trajectory simulations

The performances of the four configurations have been tested by simulating the transmission of ions through a quadrupole mass filter equipped with the corresponding rods. In the simulation the length of the filter has been set to $L = 0.15$ m, the frequency $f = 4$ MHz, the field radius $r_0 = 3 \times 10^{-3}$ m.

The results obtained by using both commercial software packages or user programs [32–35] have shown that the operation of a quadrupole mass filter is accurately described by trajectory simulations. In the present case, for a greater flexibility, a program in FORTRAN has been developed to resolve the equations of motion while the analysis of the results has been carried out by means of MATLAB procedures. The ions enter the quadrupole field with a velocity corresponding to a kinetic energy of 2.5 eV. The program generates ions in the first quadrant within a square with edges of size $r_0/2$ parallel to the positive x or y semiaxes and with a corner on the quadrupole (z) axis (see Fig. 1b). For symmetry, the same behavior is expected for ions generated in similar squares located in the other three quadrants. The square is divided in N_C equal squared subunits (SUs) and, for each SU, N_i ions are randomly generated with a uniform distribution in the SU and in the time corresponding to a period of the ac component. Therefore, a total number of particles $N = N_i \times N_C$ is injected in the field. The ion traveling time

is divided into small time intervals and their motion over each interval is computed using the local time-dependent field ϕ (Eq. (2)). The differential equations of motion are solved by using a fourth order Runge–Kutta algorithm. The time step has been decreased until no change has been observed on the results. Ions are transmitted only if their distance from the axis is less than r_0 otherwise they are lost. Ions transmitted through a length L are separately counted for each SU, their number is N_i^T. In this way it is possible to correlate the transmitted percentage of ions with the starting SU position as a function of the selected transmission mass (partial transmission $T_i = 100N_i^T/N_i$). The transmitted ions N_i^T can also be summed on the N_C SUs to obtain the (total) transmission $T = 100\sum_{N_C}(N_i^T/N)$ for each mass in order to get the transmission peak, i.e., the peak which should be experimentally measured in a mass scan by using that mass filter.

For each geometry, I have employed the appropriate series which approximates ϕ truncated to 15 terms for ORs, MRs, and PRs and truncated to 50 terms for CRs. In this way analytical partial derivatives of ϕ can be calculated and the number of terms provides sufficient accuracy. On the other hand, a direct calculation of the electric field in the simulation determines an increase of computing time with n. Therefore, I have adopted an algorithm which was originally developed for the simulation of ion trajectories in low energy ion scattering spectroscopy [36] and similar to the procedure adopted by Gibson and Taylor [37]. At the beginning of the simulation, the electric field is calculated over a dense rectangular grid of points covering the free region of radius r_0 in xy plane. Then, the electric field at the position (x, y, z) of the ion trajectory is calculated by using a bilinear interpolation of the values at the four nearest grid points of (x, y). Exploiting the symmetry of the field, only a single matrix is necessary to store both the x and y electric field components.

The transmitted mass scale for the simulation has been defined by employing the vertex of the first stability zone in the (q, a) plane [6]. In a quadrupole mass filter with field size r_0, the frequency of the ac component is generally kept constant at the resonance frequency of the system, while the mass is scanned by varying the ac amplitude V in a suitable range. The dc amplitude U is obtained rectifying a fraction of the ac component in order to keep the working point within the stability zone with a mass resolution setting which depends on the ratio $\gamma = U/V$. The vertex of the stability zone occurs at $q = 0.706$ and $a = 0.23699$ thus the transmitted mass is expressed as

$$m = \frac{4e}{0.706\omega^2 r_0^2}V \tag{4}$$

while

$$U = 0.1678\gamma V \tag{5}$$

and the numerical coefficient has been chosen such that the stability zone vertex corresponds to $\gamma = 1$. The mass scale works for a hyperbolic field ($B_0 = 1$) but for the different geometries $B_0 \neq 1$ (see Table 1) and the mass scale must be modified as

$$m\prime = B_0 \times m \tag{6}$$

taking into account that the amplitude of the $n = 0$ (hyperbolic) term has a B_0-fold increase. For instance, by using the m scale, this slight shift at low mass has been observed in the comparison between calculated hyperbolic and ORs transmission peaks [38,37]. Moreover, this shift at low mass is larger changing from hyperbolic (or ORs) to unconventional rods. This means that the voltage settings valid for a mass filter with ORs (or MRs) must be accordingly changed for the use with unconventional rods to scan the same mass range. In the following, mass values will be given in atomic mass units (amu) for a singly ionized particle.

3.1. Simulations on the optimized geometries which approximate an hyperbolic field

The first simulation runs were carried out for parameters of Table 1 corresponding to the MN_2 method and with $N_i = 3000$ and $N_C = 400$, i.e., $N = 1.2 \times 10^6$ ions, and with an initial velocity parallel to the z axis ($\chi = 0$ in Fig. 1). In Fig. 5 for an ion of mass $m_i = 28$ amu, the ratio between the number of transmitted ions and the total number of injected ions (transmission T) is shown. The filter with ORs shows a transmission which is almost twice as big as that one of mass filters with PRs or CRs. MRs results are almost identical to those of ORs, the difference are not significant and can be ascribed to fluctuations in the calculations. The transmission for CRs is slightly higher than that of PRs. Decreasing the value of γ, all the peaks broaden mainly on the low mass side. Moreover,

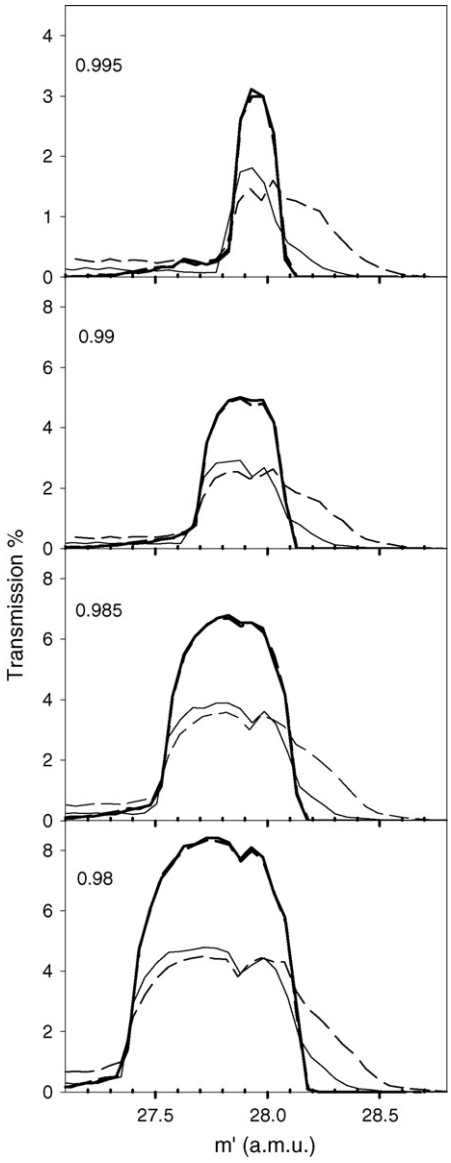

Fig. 5. Total transmission T for ion of mass $m_i = 28$ amu. Thick solid [dashed] lines refers to a mass filter equipped with ORs [MRs], thin solid [dashed] lines to one with CRs [PRs]. In each panel the value of the mass resolution γ is shown in the upper left part.

the transmission of both unconventional rods presents a tail on the high mass side which is absent for ORs and MRs. This tail, which is more pronounced for PRs, reaches $m\prime = m_i + 1$ with an intensity which is more than 2 order of magnitude less than the peak maximum. On the low mass side, all the rods show a transmission with a tail of weak intensity. For ORs and MRs this tail tends toward zero and form the initial part of the leading edge of the peak while for the other geometries the tail shows an almost constant value down to the mass $m\prime = m_i - 1$. Decreasing the mass resolution γ, this tail increases for PRs instead is almost constant or increases weakly for CRs. Previous studies on the peak shape [39] have shown that this tail is negligible in a pure hyperbolic field and the peak is almost symmetric, instead for ORs the results are similar to the the present ones and the tail makes asymmetric the peak of ORs. Moreover, the contribution of a mass m_i on the near $m\prime = m_i \pm 1$ masses can limit the abundance sensitivity which is a figure of merit that describes the ability of a mass filter to discriminate between adjacent masses of widely different intensity. Hence, the abundance sensitivity seems limited especially for the unconventional rods.

The analysis of the starting SUs which contribute to the tails are shown in Fig. 6 for $m\prime = 27.2$ amu and in Fig. 7 for the high mass side. The contour plots are obtained by mirror symmetry through the x and y axes and show the partial transmission T_i. In Fig. 6 two peaks centered on the x axis contribute to the tail on the low mass side of Fig. 5. The space with almost zero intensity between the peaks has a size $d_S \sim 0.2r_0$ for ORs and MRs, $\sim 0.16r_0$ for unconventional rods. This suggests (in agreement with Ref. [39] for ORs) that limiting the entrance region of the filter with a collimator whose size does not exceed the previous values of d_S should get rid of the tail on the low mass side. In Fig. 7, for unconventional rods, a single peak is instead present which is centered on the filter axis. In this case, any collimator centered on the axis cannot remove the high mass tail.

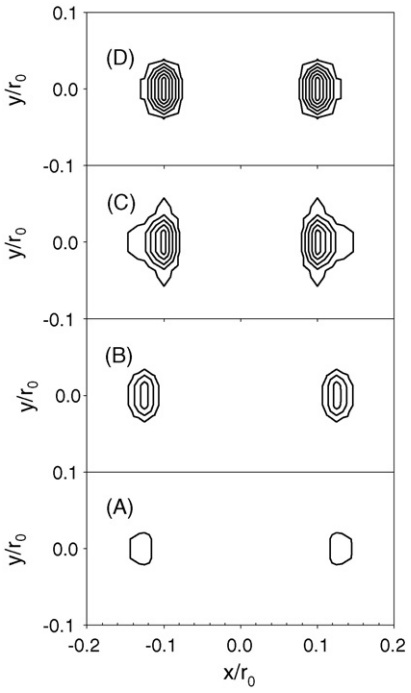

Fig. 6. Contour plots for ions of mass $m_i = 28$ amu injected in the mass filter with $\gamma = 0.99$ and $m\prime = 27.2$ amu and with different rod configurations (panel A refers to ORs, B to MRs, C to PRs, and D to CRs). The lines represent constant values of T_i, the ratio between transmitted ion starting in each SU and N_i, with 5% increment between lines.

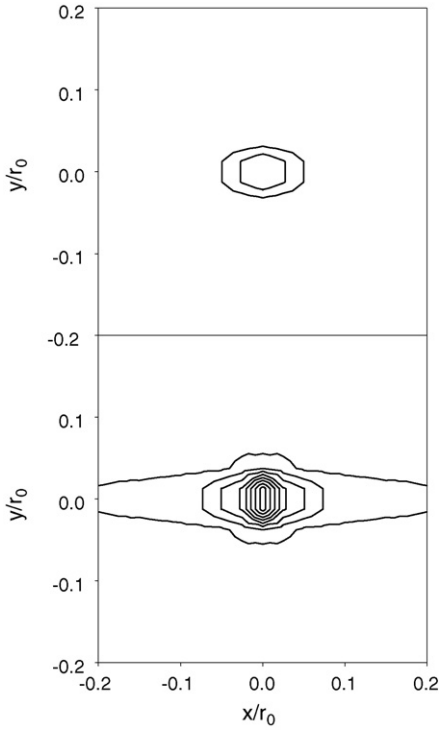

Fig. 7. Contour plots for ions of mass $m_i = 28$ amu injected in the mass filter with $\gamma = 0.99$. The lines represent constant values of T_i, the ratio between transmitted ion starting in each SU and N_i, with 1% increment between lines. The lower panel refers to a mass filter equipped with PRs at $m\prime = 28.5$ amu while upper panel to one with CRs at $m\prime = 28.4$ amu.

3.2. Simulations as a function of geometry parameters

As observed in the introduction, the best performance of a mass filter is obtained for parameters describing the geometries which are not optimized to produce an hyperbolic field. Therefore, the effect of the geometry parameters have been investigated in simulation runs with $N_i = 2160$ and $N_C = 400$, i.e., $N = 8.64 \times 10^5$ ions, with an initial velocity parallel to the z axis ($\chi = 0$ in Fig. 1b), and with the same injection region as previous simulations. The results for different geometry parameters are shown in Fig. 8 for ORs; in Fig 9 for MRs; in Fig. 10 for PRs; in Fig. 11 for CRs. In the panel (a), the total transmission is shown for $\gamma = 0.9995$ while in the panels (b) and (c) the corresponding mass resolution $m/\Delta m$ (at 50% or 10% of the peak transmission) and the maximum transmission are depicted for $\gamma = 0.9995$ and 0.995.

In agreement with the results of Ref. [39], the peak for ORs (Fig. 8a) and simulated for $\gamma = 0.9995$ decreases in intensity going from $r/r_0 = 1.100$ to 1.160 while its width Δm at first decreases and then increases again. The mass resolution $m/\Delta m$ (Fig. 8b) is not peaked at the parameter values corresponding to optimized geometry of Table 1 but at smaller values, between 1.120 and 1.130 for $m/\Delta m$ at 10% and between 1.125 and 1.130 for that one at 50%. In these regions also the maximum of the transmission peak (Fig. 8c) is higher than that one of the optimized geometry. The comparison with simulations performed for $\gamma = 0.995$ shows that, apart an expected increased transmission, the $m/\Delta m$ curve is almost flat, i.e., only for enough resolved peak there is a dependence on the parameter values. The low mass tail is absent for 1.100 and its intensity increases with the parameter value. Moreover, it shows a small peak whose m' position decreases in mass increasing the parameter value. No high mass tail is present. The mass resolution at 10% displays a sharp drop between 1.130 and

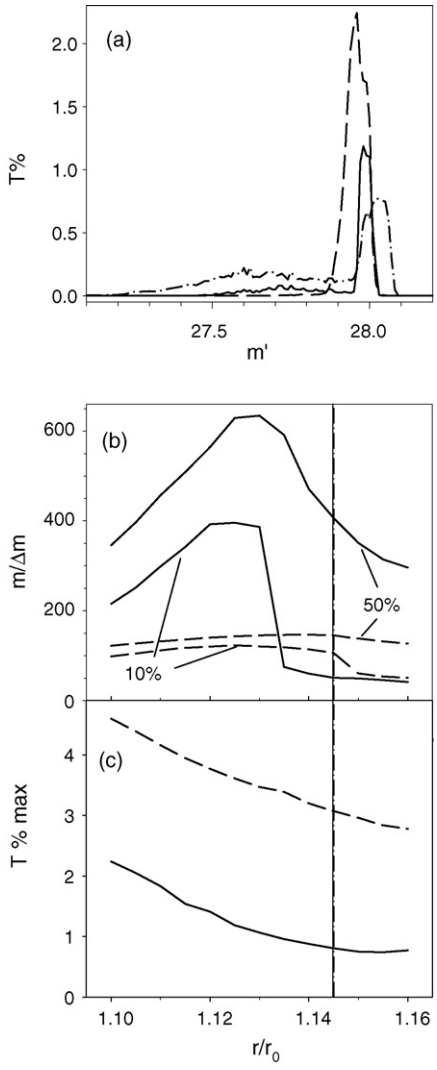

Fig. 8. (Panel a): total transmission for ions of mass $m_i = 28$ amu injected in a mass filter equipped with ORs and $\gamma = 0.9995$ for different parameters r/r_0: 1.100 (dashed line), 1.125 (solid line), 1.160 (dot-dashed line). (Panel b): mass resolution $m/\Delta m$ evaluated at 50% or 10% of the mass peak. (Panel c): maximum of the mass peak. For panels (b) and (c) dashed lines correspond to $\gamma = 0.995$ and solid lines to $\gamma = 0.9995$. The almost coincident vertical lines mark the parameters of the optimized geometries obtained with the MN_2 (solid line) or the VB_1 (dash-dotted line) methods.

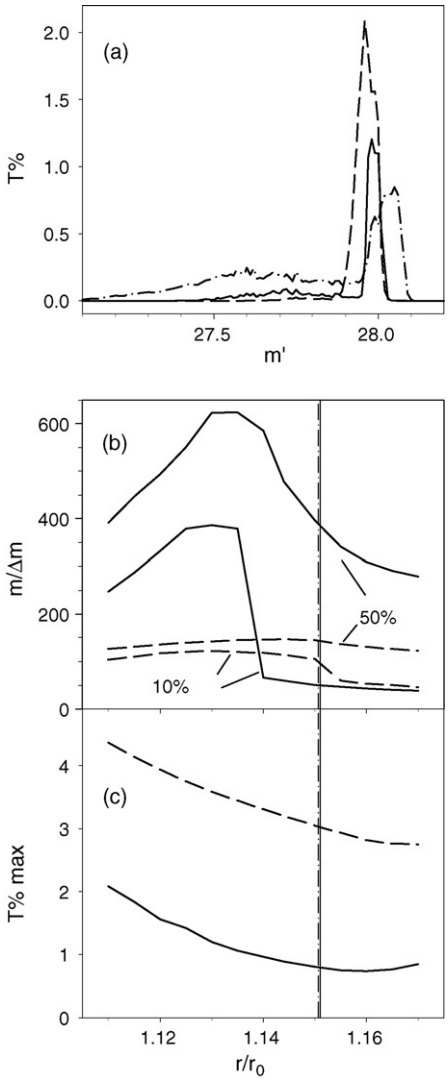

Fig. 9. (Panel a): total transmission for ions of mass $m_i = 28$ amu injected in a mass filter equipped with MRs and $\gamma = 0.9995$ for different parameters r/r_0: 1.110 (dashed line), 1.130 (solid line), 1.170 (dot-dashed line). (Panel b): mass resolution $m/\Delta m$ evaluated at 50% or 10% of the mass peak. (Panel c): maximum of the mass peak. For panels (b) and (c) dashed lines correspond to $\gamma = 0.995$ and solid lines to $\gamma = 0.9995$. The vertical lines mark the parameters of the optimized geometries obtained with the MN_2 (solid line) or the VB_1 (dash-dotted line) methods.

1.135 due to the low mass tail which broadens the foot of the peak.

For MRs (Fig. 9), the trend is very similar to ORs. The differences are in the $m/\Delta m$curve, whose maximum is slight decreased and extended to an interval between 1.130 and 1.135 for the curve at 50% (1.125 and 1.135 for that one at 10%), and in the transmission which is slightly higher than that of ORs for $r/r_0 < 1.135$.

In Fig. 10 a, the peaks of PRs show a larger variation of the maximum transmission with respect to ORs. The low mass tail increases with d/r_0 and for 1.00 is about 5-fold the value at 0.80. The peak position depends on the parameter d and the B_0 correction on the mass is not sufficient to block the peak around $m' = 28$. In panel (b) and $\gamma = 0.9995$, the peak width at 50% has a minimum at $d/r_0 = 0.80$ very close to the minimum of the transmission: the mass resolution is 2/3 and the transmission values are about 3/4 of the corresponding values of ORs. The $m/\Delta m$ peak shows a sharp drop between 0.80 and 0.82 due to the high mass tail. Between 0.82 and 0.84 the low mass tail contribution further enlarges the peak width below $m' = 26.5$, the starting mass of the present simulations; therefore, the resolution has been set to zero. From this point on, the transmission structure is formed essentially by the tails. The resolution $m/\Delta m$ at 10% shows a maximum at $d/r_0 = 0.78$ and a value which is 1/3 of the corresponding value for ORs. In this case the sharp drop between 0.78 and 0.80 is due to the low and high mass tails. For $\gamma = 0.995$, the mass resolution curves are not flat as in the case of ORs, but their variations are reduced with respect to the curves at higher γ. Also in the case of PRs, the mass resolution $m/\Delta m$ (Fig. 10b) is not peaked at the parameter values corresponding to optimized geometry of Table 1 but at smaller values. Moreover, the low mass tail also presents some small features which modulates the average value of the tail.

For CRs (Fig. 11a), the appearance is similar to the previous figure. Also in this case, the peak position depends on the parameter A. There are low and high mass tails, but, in particular when the width is close to the minimum, the low mass tail has a transmission comparable with that of the peak. Moreover, in a more clearly

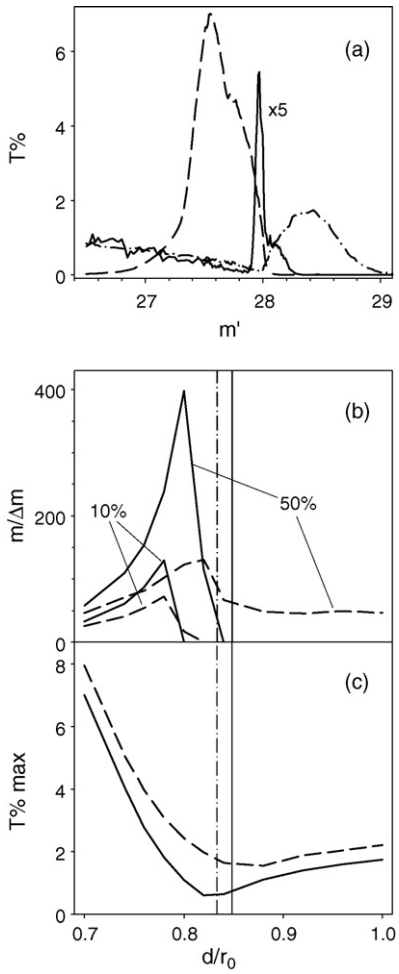

Fig. 10. (Panel a): total transmission for ions of mass $m_i = 28$ amu injected in a mass filter equipped with PRs and $\gamma = 0.9995$ for different parameters d/r_0: 0.7 (dashed line), 0.8 (solid line), 1.0 (dot-dashed line). (Panel b): mass resolution $m/\Delta m$ evaluated at 50% or 10% of the mass peak. (Panel c): maximum of the mass peak. For panels (b) and (c) dashed lines correspond to $\gamma = 0.995$ and solid lines to $\gamma = 0.9995$. The vertical lines mark the parameters of the optimized geometries obtained with the MN_2 (solid line) or the VB_1 (dash-dotted line) methods.

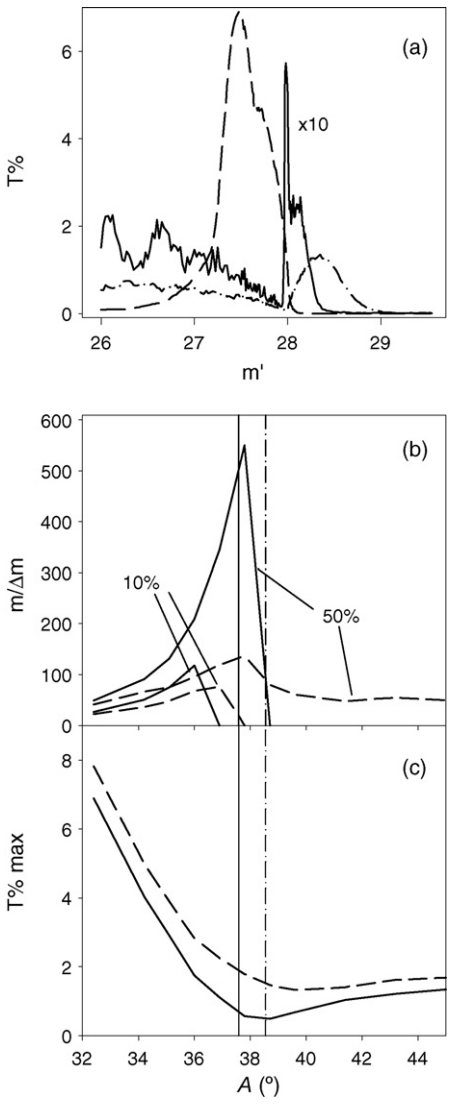

Fig. 11. (Panel a): total transmission for ions of mass $m_i = 28$ amu injected in a mass filter equipped with CRs and $\gamma = 0.9995$ for different parameters A: 32.4° (dashed line), 37.8° (solid line), 45.0° (dot-dashed line). (Panel b): mass resolution $m/\Delta m$ evaluated at 50% or 10% of the mass peak. (Panel c): maximum of the mass peak. For panels (b) and (c) dashed lines correspond to $\gamma = 0.995$ and solid lines to $\gamma = 0.9995$. The vertical lines mark the parameters of the optimized geometries obtained with the MN_2 (solid line) or the VB_1 (dash-dotted line) methods.

way than the PRs case, the figure shows that the low mass tail is structured and presents some features that could be interpreted as further peaks in a mass scan. The $m/\Delta m$ curve at 50% has a maximum between the positions corresponding to the values obtained with the MN_2 and VB_1 methods which also correspond to the minimum of the transmission. The sharp drop between 38° and 39° is due to the low mass tail which extends below $m' = 26$, the starting mass of the present simulations; therefore, the resolution has been set to zero. The same happens for the two 10% curves. The mass resolution is greater than that one of PRs but less than those ones of MRs and ORs, and for the maximum of the resolution the transmission is lower than that one of PRs and is about 0.6 times those ones of ORs and MRs.

For a complete analysis of the performances, other simulations have also been carried out to investigate the dependence on the injection angle χ. In fact, ions are injected in a mass filter by means of a lens assembly that determines the focusing of their trajectories near the entrance of the filter thus initial particle velocities generally are not parallel to the filter axis. The geometry of the lens assembly and its voltage setting determine the converging shape of the cone formed by the ion trajectories at filter entrance. To gain insights on the behavior of the mass filter in this case, the simulations have been carried out, for any geometry parameter, at the masses m' corresponding to the maximum in the total transmission and for different azimuthal direction θ between 0° (x axis) and 90° (y axis) in steps of 15° and with distances ρ from the axis in the range $0.0125r_0$ and $0.5r_0$ in steps of $0.0125r_0$. For each direction and position, the ions have been injected in the field for χ in the range −15° and +15° with a 3° step. Negative χ angles correspond to trajectories converging toward the quadrupole axis while positive ones to trajectories diverging from the axis. For each kinematical condition (ρ, θ, χ), $N_a = 10^4$ ions have been randomly injected with a uniform distribution in the time corresponding to a period of the ac component and the partial transmission T_a has been calculated as the ratio between transmitted ions and N_a. Within the fluctuations of the calculations, the results for negative angles are equal to those with positive angles, therefore, only results for positive angles will be shown.

An example of the results about T_a is shown in Fig 12 for ORs. The chosen geometry correspond to that one which provides the

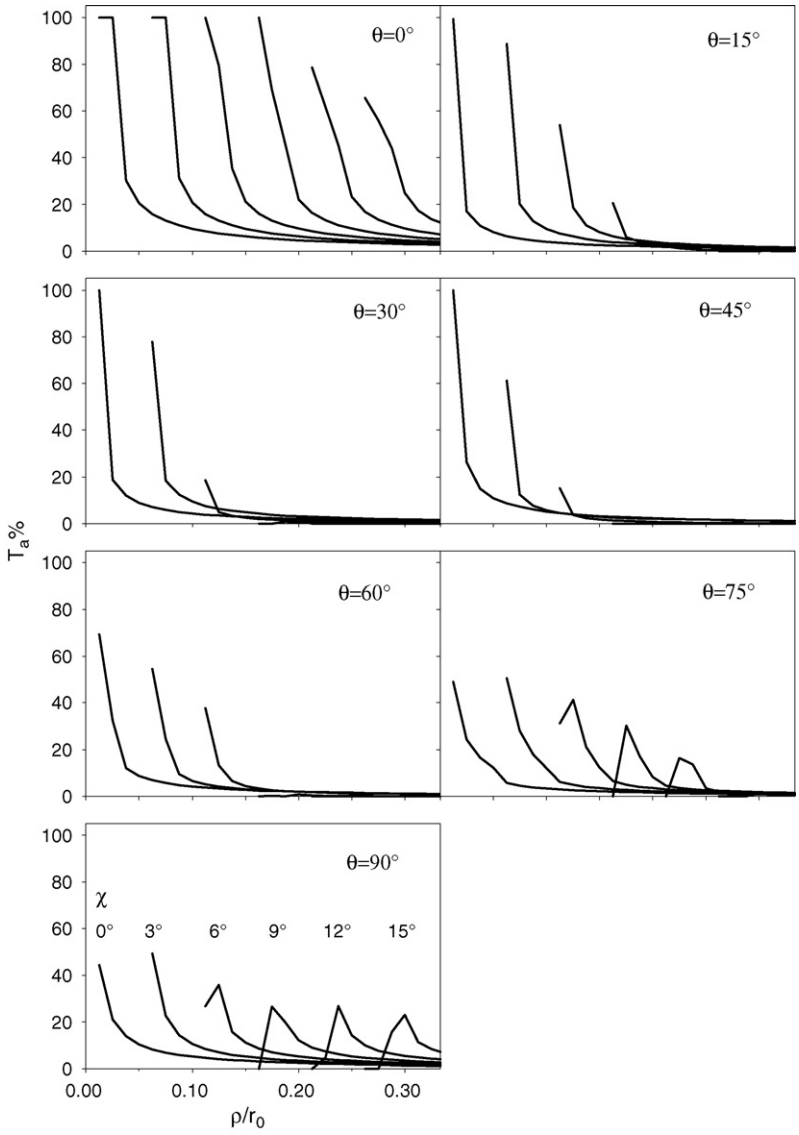

Fig. 12. Partial transmission for ions of mass $m_i = 28$ amu injected along different azimuthal directions θ in a mass filter equipped with ORs and $\gamma = 0.9995$ and $r/r_0 = 1.125$. Each curve corresponds to ions injected with different polar angle χ in the range from 0° to 15°. Each curve is shifted of a constant amount $\rho = 0.05r_0$ with increasing χ.

best mass resolution as discussed above. As a general trend, all T_a curves are decreasing function of ρ, except for $\theta = 75°$ and 90° where maxima away from $\rho = 0$ are also present. The transmission values along the x axis ($\theta = 0°$) are greater than the ones in the other azimuthal directions. As expected, increasing χ, the transmission decreases to zero.

The results for ORs and MRs (not shown) are very similar. Along $\theta = 0°$, the ions are 100% transmitted for $\rho < 0.025r_0$ up to $\chi = 3°$. For greater distances the transmission decreases to zero almost as ρ^{-1}. Increasing χ to 9°, the transmission is still 100% for $\rho \leq 0.0125r_0$. Along the other azimuthal directions, the transmission over 50% is limited to $\chi \leq 3°$ and $\rho < 0.025r_0$. Along $\theta = 90°$, the transmission of ions injected at $\chi = 15°$ is higher than 20% around $\rho = 0.05r_0$.

The results (not shown) for PRs and CRs are similar along $\theta = 0°$, but for the other directions the transmission of PRs is higher than the corresponding one of CRs. The results for PRs also show that the 100% transmission along $\theta = 0°$ is possible up to $\chi = 15°$ and $\rho < 0.05r_0$. At $\theta = 15°$ and 30° the transmission is lower than that one of ORs, but for $\theta \geq 60°$ the transmission is slightly higher.

In order to easily compare the behavior of the four configurations as a function of the geometry parameters, T_a values for $\chi = 0°$, 6°, and 12° at $\rho = 0.0125r_0$ and along $\theta = 0°$, 45°, 90° have been depicted in Fig. 13 for ORs; in Fig. 14 for MRs; in Fig. 15 for PRs; and in Fig. 16 for CRs. Moreover, also the trend for $\chi = 12°$ and $\rho = 0.05r_0$ is shown.

In Fig. 13, along $\theta = 0°$ and at $\rho = 0.0125r_0$, the transmission is 100% for $\chi = 0°$ and 6° while for 12° increases from 60% up to 100% around the parameter values corresponding to the optimized geometry. Along $\theta = 45°$, only for $\chi = 0°$ a 100% transmission is obtained for $r/r_0 \leq 1.125$, otherwise the transmission has a decreasing trend and the curves for $\chi = 0°$ and 6° have a similar negative slope. Moreover, for $\chi = 6°$, the transmission vanishes around $r/r_0 = 1.14$ and, for $\chi = 12°$, it vanishes around $r/r_0 = 1.12$. Along $\theta = 90°$, T_a presents a minimum for all the curves at $r/r_0 = 1.15$, close to the optimized geometry. The T_a values decrease twice passing from $\chi = 0°$ to 6° and they vanish for $\chi = 12°$.

Analyzing the trend at $\rho = 0.05r_0$ and $\chi = 12°$, along $\theta = 0°$, T_a shows a maximum at $r/r_0 = 1.15$ which is less than 40%. Along $\theta = 45°$, T_a is essentially zero. Along $\theta = 90°$, T_a is always greater than 10% and shows a minimum at $r/r_0 = 1.15$, similarly to the other

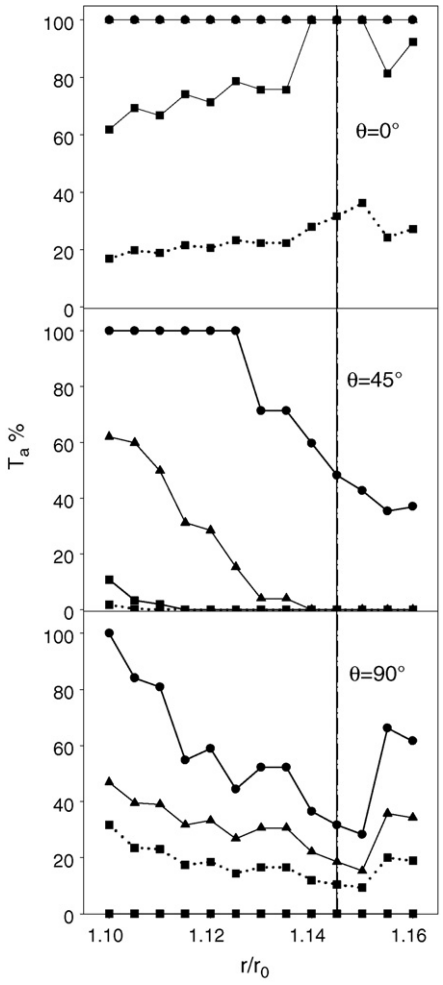

Fig. 13. Partial transmission as a function of r/r_0 for ions of mass $m_i = 28$ amu injected along $\theta = 0°, 45°$, and $90°$ in a mass filter equipped with ORs and $\gamma = 0.9995$. The solid lines are the results of simulations performed at $\rho/r_0 = 0.0125$ and polar angles $\chi = 0°$ (solid circles) $6°$ (solid triangles), $12°$ (solid squares). The dashed line with solid squares corresponds to $\rho/r_0 = 0.05$ and $\chi = 12°$. The vertical lines mark the parameters of the optimized geometries obtained with the MN_2 (solid line) or the VB_1 (dash-dotted line) methods.

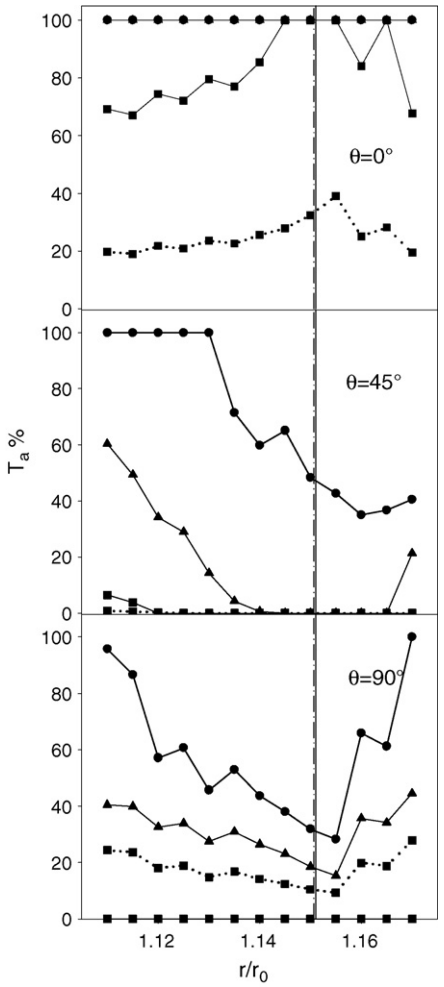

Fig. 14. Partial transmission as a function of r/r_0 for ions of mass $m_i = 28$ amu injected along $\theta = 0°$, $45°$, and $90°$ in a mass filter equipped with MRs and $\gamma = 0.9995$. The solid lines are the results of simulations performed at $\rho/r_0 = 0.0125$ and polar angles $\chi = 0°$ (solid circles) $6°$ (solid triangles), $12°$ (solid squares). The dashed line with solid squares corresponds to $\rho/r_0 = 0.05$ and $\chi = 12°$. The vertical lines mark the parameters of the optimized geometries obtained with the MN_2 (solid line) or the VB_1 (dash-dotted line) methods.

curves at $\rho = 0.0125r_0$. This non-zero behavior for $\theta = 90°$ is related to the peak around $\rho = 0.05r_0$ observed in the lower panel of Fig. 12, which is present for all the range of simulated parameter values.

The transmission curves for MRs (Fig. 14) are very similar to those ones of ORs and the values differ for a few percent therefore the previous description applies also to MRs. The transmission maxima and minima are shifted of $0.005r_0$ which is consistent with the shift in Table 1 between the parameters for the optimized geometry of ORs and MRs and the shift between the corresponding $m/\Delta m$ curves.

For PRs (Fig. 15), the transmission along $\theta = 0°$ at $\rho = 0.0125r_0$ is 100% for χ up to $12°$. Along $\theta = 45°$, the curves for $\chi = 0°$ and $6°$ start at 100% at $d/r_0 = 0.7$ and present a minimum at $d/r_0 = 0.82$ where the curve for $\chi = 6°$ almost vanishes. At $d/r_0 = 1$, the curve for $\chi = 0°$ recovers the 100% transmission instead the curve for $\chi = 6°$ reaches only a transmission of almost 60%. The curve for $\chi = 12°$ starts at about 80% at $d/r_0 = 0.7$, vanishes at $d/r_0 = 0.8$ and the transmission remains negligible up to $d/r_0 = 1$. Along $\theta = 90°$, the behavior is similar to that one along $\theta = 45°$: the curve for $\chi = 0°$ recovers quickly the 100% transmission after the minimum at 0.82 and the curve for $\chi = 6°$ does not vanish at the minimum and for $d/r_0 > 0.86$ reaches an almost constant value around 65%. The curve for $\chi = 12°$ starts at about 50% at $d/r_0 = 0.7$, vanishes between $d/r_0 = 0.76$ and 0.82 and then reaches an almost constant value around 25%. For this configurations, minima happen at the parameter value corresponding to the maximum of the mass resolution (Fig. 10). Along $\theta = 0°$, the curve at $\rho = 0.05r_0$ and $\chi = 12°$ oscillates around 80% with a maximum at $d/r_0 = 0.82$ and a minimum at $d/r_0 = 0.88$. Along $\theta = 45°$ and for $d/r_0 < 0.8$, the curve decreases with a smaller transmission values than the curve at the same χ angle and $\rho = 0.0125r_0$ but it displays greater values for $d/r_0 > 0.82$, and, at $d/r_0 = 1$, it reaches about 15%. Along $\theta = 90°$, the curve shows a minimum at 0.82 and then levels off at a constant value of about 40%.

For CRs (Fig. 16), the curves show a trend which is similar to that of PRs. In fact, the transmission along $\theta = 0°$ at $\rho = 0.0125r_0$ is 100% for χ up to $12°$. Along $\theta = 45°$, the curves for $\chi = 0°$ and $6°$ start at 100% at $A = 32°$ and present a minimum at $A = 39°$ and $38°$, respectively. There, the curve for $\chi = 6°$ almost vanishes. At $A = 45°$, the curve for $\chi = 0°$ reaches almost 95% transmission instead the curve for $\chi = 6°$ only 50%. The curve for $\chi = 12°$ starts almost at 90% at $A = 32°$, vanishes at $A = 37°$ and the transmission remains negligible up to $A = 45°$. Along $\theta = 90°$, the behavior is similar to that

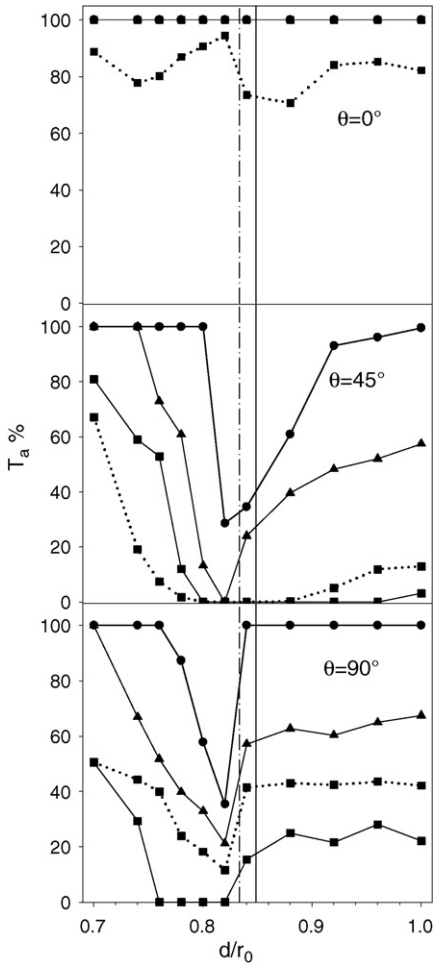

Fig. 15. Partial transmission as a function of d/r_0 for ions of mass $m_i = 28$ amu injected along $\theta = 0°$, 45°, and 90° in a mass filter equipped with PRs and $\gamma = 0.9995$. The solid lines are the results of simulations performed at $\rho/r_0 = 0.0125$ and polar angles $\chi = 0°$ (solid circles) 6° (solid triangles), 12° (solid squares). The dashed line with solid squares corresponds to $\rho/r_0 = 0.05$ and $\chi = 12°$.

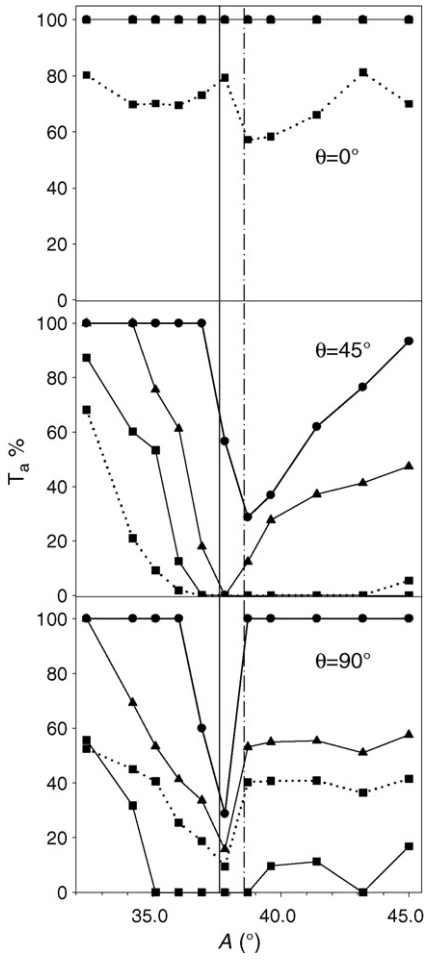

Fig. 16. Partial transmission as a function of A for ions of mass $m_i = 28$ amu injected along $\theta = 0°$, 45°, and 90° in a mass filter equipped with CRs and $\gamma = 0.9995$. The solid lines are the results of simulations performed at $\rho/r_0 = 0.0125$ and polar angles $\chi = 0°$ (solid circles) 6° (solid triangles), 12° (solid squares). The dashed line with solid squares corresponds to $\rho/r_0 = 0.05$ and $\chi = 12°$. The vertical lines mark the parameters of the optimized geometries obtained with the MN_2 (solid line) or the VB_1 (dash-dotted line) methods.

one along $\theta = 45°$, the difference is the position of the minimum at $A = 38°$ which is common for the curves at $\chi = 0°$ and 6°. After the minimum, the curve for $\chi = 0°$ recovers quickly the 100% transmission and the curve for $\chi = 6°$ does not vanish at the minimum and for $A > 39°$ levels off to an almost constant value around 55%. The curve for $\chi = 12°$ starts at about 55% at $A = 32°$ and vanishes between $A = 35°$ and 39°. Then the curve presents a maximum and vanishes again at about $A = 43°$. Also in this case, minima happen at the parameter value corresponding to the maximum of the mass resolution (Fig. 11) which is close to the parameter for the optimized geometry with MN_2 method. Along $\theta = 0°$, the curve at $\rho = 0.05r_0$ and $\chi = 12°$ shows the same type of oscillations as that one of PRs but around 70% with a maximum at $A = 38°$ and a minimum at $A = 39°$. Along $\theta = 45°$, the curve has a trend similar to the curve at the same χ angle and $\rho = 0.0125r_0$ but with a smaller transmission values for $d/r_0 < 37°$. Along $\theta = 90°$, the curve shows a minimum at $A = 38°$ and then reaches almost a constant value around 40%.

3.3. Simulations for a restricted injection

The results of the previous sections have shown that the performances of the filters are affected by low mass tails and, for unconventional rods PRs and Crs, also by high mass ones. In particular, low mass tails are produced by trajectories which originate in two regions symmetrically placed around the quadrupole axis and along the x axis (Fig. 6). Also the study of the ion injection with initial velocity non-parallel to the quadrupole axis ($\chi \neq 0$) indicates that for $\rho > 0.1r_0$ the partial transmission T_a is less than 10%. Hence, a restriction of the injection area should be beneficial for high transmission also for focused trajectories and for better abundance sensitivity. Therefore, simulations have been performed injecting $N_r = 9.216 \times 10^4$ ions with $\chi = 0°$ into an injection area limited to a square initially with edges $d_S = 0.2r_0$ and then, for sake of comparison, with edges $d_S = 0.1r_0$ around the quadrupole axis. The simulations have also been performed on mass $m_i = 84$ amu to compare the performances on two different masses. The results of these simulations are shown in Fig. 17 for ORs, in Fig. 18 for MRs, in Fig. 19 for PRs, and in Fig. 20 for CRs. As expected, the transmission increases for all the configurations because the collimation excludes regions with poor partial transmission. Moreover, the tail at low mass almost disappears for $d_S = 0.2r_0$ and is totally absent for $0.1r_0$.

For ORs (Fig. 17 c1) and $d_S = 0.2r_0$, the mass resolution at 50% for $m = 28$ has a trend similar to that one of Fig. 7 while for $m = 84$ the peak has an higher value with a maximum at $r/r_0 = 1.130$. On the other hand, for $d_S = 0.1r_0$ the curves for different masses present the same behavior with a maximum at 1.125. Therefore, in Fig. 17a

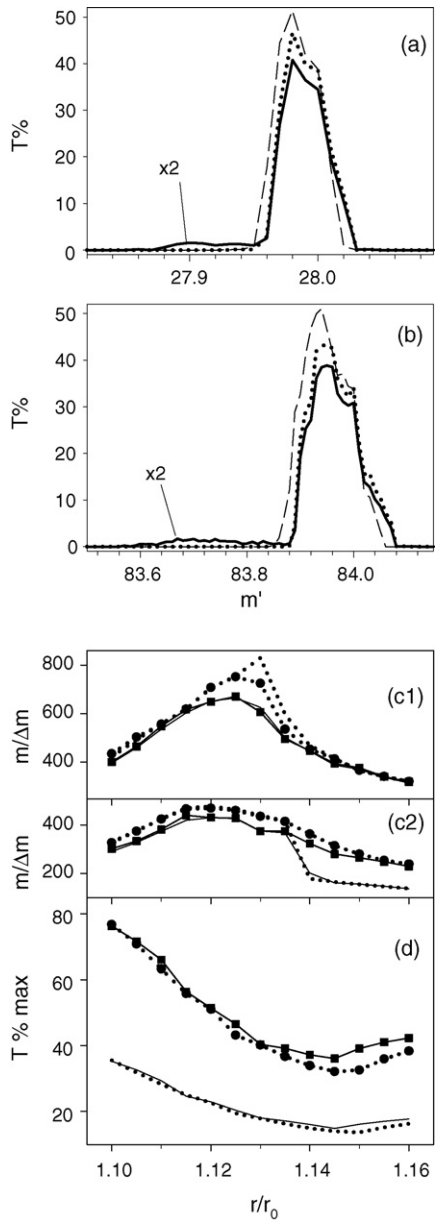

Fig. 17. Total transmission for ions of mass $m_i = 28$ amu (panel a) and $m_i = 84$ amu (panel b) injected through a square of edge $0.2r_0$ [$0.1r_0$] in a mass filter equipped with ORs, $\gamma = 0.9995$, and $r/r_0 = 1.125$ (thick solid line) [dotted lines]. The thick lines have been multipled by 2. Total transmission in a filter with $r/r_0 = 1.120$ are also depicted (dashed lines). (Panel c): mass resolution $m/\Delta m$ evaluated at 50% (c1) or 10% (c2) of the mass peak. (Panel d): maximum of the mass peak. For panels (c) and (d) solid lines correspond to $m = 28$ amu and dotted lines to $m_i = 84$ amu, lines with [without] symbols (square for $m = 28$ and circles for $m = 84$) to simulations carried out with $d_S = 0.1r_0$ [$d_S = 0.2r_0$].

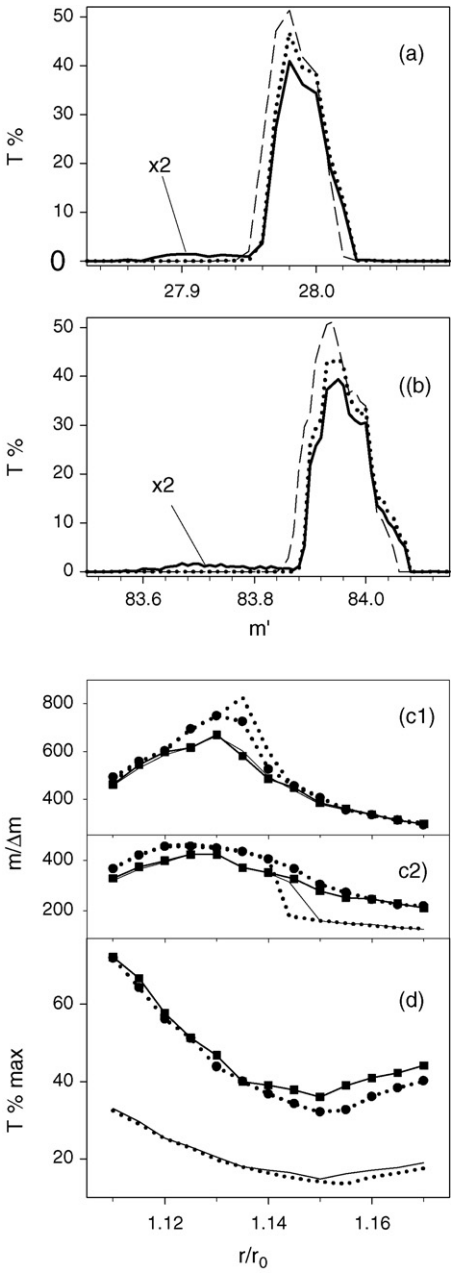

Fig. 18. Total transmission for ions of mass $m_i = 28$ amu (panel a) and $m_i = 84$ amu (panel b) injected through a square of edge $0.2r_0$ [$0.1r_0$] in a mass filter equipped with MRs, $\gamma = 0.9995$, and $r/r_0 = 1.130$ (thick solid line)[dotted lines]. Thick lines have been multiplied by 2. Total transmission in a filter with $r/r_0 = 1.125$ are also depicted (dashed lines). (Panel c): mass resolution $m/\Delta m$ evaluated at 50% (c1) or 10% (c2) of the mass peak. (Panel d): maximum of the mass peak. For panels (c) and (d) solid lines correspond to $m = 28$ amu and dotted lines to $m = 84$ amu, lines with [without] symbols (square for $m = 28$ and circles for $m = 84$) to simulations carried out with $d_S = 0.1r_0$ [$d_S = 0.2r_0$].

and b the transmissions at $r/r_0 = 1.125$ are shown. The curves for $d_S = 0.2r_0$ present a small low mass tail with a maximum around $m' = 27.9$ and 83.7 amu, respectively. Decreasing the injection area to $d_S = 0.1r_0$ the peak transmission increases more than a factor 2 retaining the same peak shape and the low mass tail completely disappears. The mass resolution at 10% (Fig. 17 c2) has a maximum at $r/r_0 = 1.120$ and in panels a and b the corresponding peaks are also reported. The peak width is slightly larger than that one at 1.125 but there is about 10% more transmission. Decreasing the injection to $0.1r_0$ the mass resolution show a more gradual change because the low mass tail vanishes and the sharp decrease between 1.135 and 1.140 disappears. The transmission in panel d doubles from $d_S = 0.2r_0$ to $0.1r_0$. The curve corresponding to $m = 28$ is on average above the one for $m = 84$. The difference is particularly evident for $r/r_0 > 1.130$ and increases by decreasing d_S.

In the case of MRs (Fig. 18), the behavior is very similar to that one of ORs. The mass resolution curves at 50% display maxima which are shifted to $r/r_0 = 1.130$, instead at 10% the maximum is around 1.125. For $r/r_0 < 1.135$, the transmission is more than 5% higher than that of ORs and shows an evident mass dependence for $r/r_0 > 1.135$.

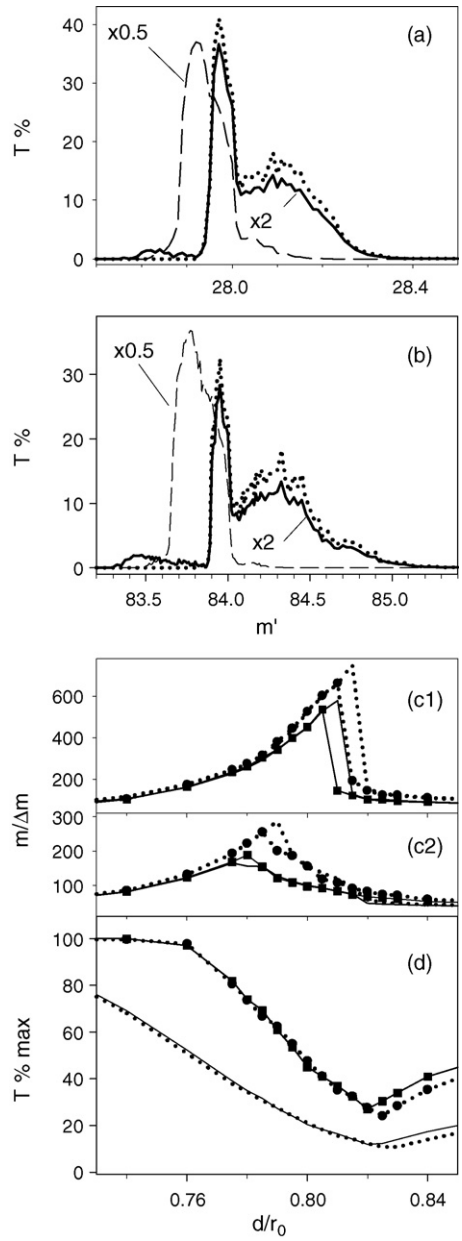

Fig. 19. Total transmission for ions of mass $m_i = 28$ amu (panel a) and $m_i = 84$ amu (panel b) injected through a square of edge $0.2r_0$ [$0.1r_0$] in a mass filter equipped with PRs, $\gamma = 0.9995$, and $d/r_0 = 0.805$ (thick solid line) [dotted lines]. Thick lines have been multiplied by 2. Total transmission in a filter with $d/r_0 = 0.780$ are also depicted (dashed lines divided by 2). (Panel c): mass resolution $m/\Delta m$ evaluated at 50% (c1) or 10% (c2) of the mass peak. (Panel d): maximum of the mass peak. For panels (c) and (d) solid lines correspond to $m = 28$ amu and dotted lines to $m = 84$ amu, lines with [without] symbols (square for $m = 28$ and circles for $m = 84$) to simulations carried out with $d_S = 0.1r_0$ [$d_S = 0.2r_0$].

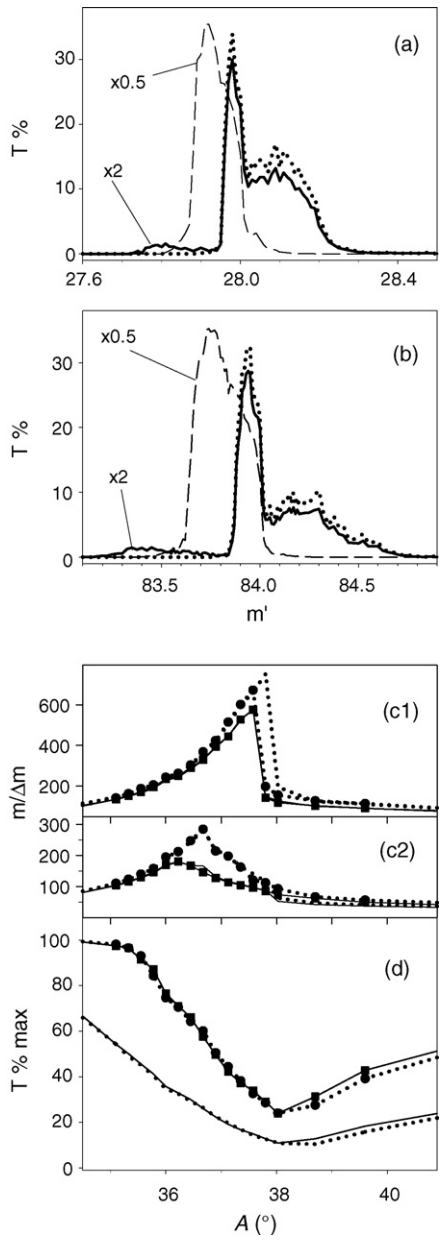

Fig. 20. Total transmission for ions of mass $m_i = 28$ amu (panel a) and $m_i = 84$ amu (panel b) injected through a square of edge $0.2r_0$ [$0.1r_0$] in a mass filter equipped with CRs, $\gamma = 0.9995$, and $A = 37.575°$ (thick solid line) [dotted lines]. Thick lines have been multiplied by 2. Total transmission in a filter with $A = 36.225°$ are also depicted (dashed lines divided by 2). (Panel c): mass resolution $m/\Delta m$ evaluated at 50% or 10% of the mass peak. (Panel c): maximun of the mass peak. For panels (c) and (d) solid lines correspond to $m = 28$ amu and dotted lines to $m = 84$ amu, lines with [without] symbols (square for $m = 28$ and circles for $m = 84$) to simulations carried out with $d_S = 0.1r_0$ [$d_S = 0.2r_0$].

For PRs (Fig. 19) the mass resolution at 50% has a maximum at $d/r_0 = 0.810$ (0.815) for $d_S = 0.2r_0$ and $m = 28$ ($m = 84$) which shifts at 0.805 (0.810) for $d_S = 0.1r_0$ leaving unaltered the leading edge of the curves. This shift at a lower value can be explained by considering the total transmission curves at the maximum of $m/\Delta m$ (panels a and b) which show a peak with a tail on the high mass side (which for $m_i = 84$ reaches $m' = 85$) having a transmission slightly below 50% of the peak transmission. Decreasing d_S the tail acquires a greater relative intensity and crosses the 50% of the peak transmission determining a sharp decreasing of $m/\Delta m$ with the shift to the left of the $m/\Delta m$ maximum. Instead the trend of $m/\Delta m$ at 10% has a more regular trend and the changes between $d_S = 0.2_0$ and $0.1r_0$ are negligible. The maximum is located around $d/r_0 = 0.780$ for $m = 28$ and around 0.785 for $m = 84$. The peaks which correspond to $d/r_0 = 0.780$ (depicted in panels a and b) present a reduced or negligible high mass tail and a better overall shape with respect to the peaks related to the maxima at 50% and with about a doubling of the transmission ($> 70\%$). Therefore, in spite of a larger width, d/r_0 in the range between 0.780 and 0.785 could be the right choice to attain a more definite peak shape with high transmission. For $d/r_0 > 0.820$, the transmission shows an evident mass dependence and the difference

between the two masses increases passing from $d_S = 0.2r_0$ to $0.1r_0$.

For CRs (Fig. 20 c1) the mass resolution at 50% has a maximum at $A = 37.575^\circ$ (37.800°) for $d_S = 0.2r_0$ and $m = 28$ ($m = 84$). For $d_S = 0.1r_0$, the curve does not change for $m = 28$ while for $m = 84$ the leading edge of the curve is unaltered and there is a small shift of the maximum which coincides for both masses around $A = 37.575^\circ$. As in the case of PRs, the peaks which correspond to those maxima (panels a and b) present a tail on the high mass side having an intensity slightly below 50% of the peak transmission. Decreasing d_S the tail acquires a greater relative intensity only for $m = 84$ determining the shift of the maximum position. With respect to PRs, the high mass tail covers a more limited mass range, but there are small peaks, not present in the case of PRs, also for $m' > m_i + 1$ with a transmission below 0.01%. The $m/\Delta m$ curves at 10% (panel c2) do not show any significant change between the two d_S values. The maximum is at $A = 36.225^\circ$ for $m = 28$ and $A = 36.675^\circ$ for $m = 84$. Similarly to PRs, the peaks which correspond to $A = 36.225^\circ$ (depicted in panels a and b) present a reduced or negligible high mass tail and a better overall shape with respect to the peaks related to the maxima at 50% of the peak transmission and with about a doubling of the transmission ($> 70\%$). Therefore, in spite of a larger width, A in the range between 36.23° and 36.68° could be the right choice to attain a more definite peak shape with high transmission. For $A > 38^\circ$, the transmission shows a smaller but evident mass dependence and the difference between the two masses increases passing from $d_S = 0.2r_0$ to $0.1r_0$.

4. Conclusions

In this article the performance of mass filters equipped with rods of different convexity has been investigated. The optimized geometries which best approximate the hyperbolic field have been determined by calculations based on a finite elements approach. Trajectory simulations have been employed to determine the comparative performance of mass filters equipped with these rods. The restriction of the injection area to $d_S = 0.1r_0$ completely eliminates the low mass tail for all the configurations. High mass tail, which is not present for ORs and MRs, determine broader peaks for PRs and CRs: even restricting the area to $d_S = 0.1r_0$, for PRs the tail extends up to $m + 1$ and, in the case of CRs, small peaks are present for $m' > m + 1$ with a transmission smaller than 0.01%. Those are limits to the abundance sensitivity of mass filters equipped with PRs or CRs. The study of small changes around the optimized geometries have confirmed also for non-conventional geometries that better mass resolution and transmission are obtained for parameters which are smaller then the optimized ones. Decreasing the geometry parameters with respect to optimized ones, the transmission increases for all the configurations. The trends of mass resolution curve at 50% and 10% of the transmission peak show maxima located at different positions and there is also a weak dependence on the ion mass. Considering 50% curve for a restricted injection $d_S = 0.1r_0$ of $m = 28$ ions, the central position of the maximum is $r/r_0 = 1.125$ for ORs, $r/r_0 = 1.130$ for MRs, $d/r_0 = 0.805$ for PRs, and $A = 37.58^\circ$ for CRs, i.e., -1.8% for ORs and MRs, -3.4% for PRs, and -2.5% for CRs with respect the optimized values obtained with the VB_1 method (Table 1). Instead, considering 10% curves, the central position of the maximum is $r/r_0 = 1.120$ for ORs, $r/r_0 = 1.125$ for MRs, $d/r_0 = 0.780$ for PRs, and $A = 36.23^\circ$ for CRs, i.e., -2.2% for ORs and MRs, -6.4% for PRs, and -6.0% for CRs with respect the optimized values obtained with the VB_1 method.

Curves at 10% are more sensitive to the presence of tails and the parameters related to their maxima could be a useful guide for practical constructions to obtain higher transmissions and, for unconventional rods, a better shape of the transmission peaks. In spite of higher transmission values (70% for PRs and CR with respect to 50% for ORs and MRs), only convex configurations, ORs and MRs, meet the requirements of better mass resolution and abundance sensitivity. Moreover, when also size and weight are important parameters, the better choice for compact mass filters is the use of modified cylindrical rods.

Acknowledgements

The author thanks R. Tatarek and L. Pedemonte for helpful discussions.

References

[1] W. Paul, H. Steinwedel, Z. Naturforsch. A8 (1953) 448.
[2] W. Paul, M. Raether, Z. Phys. 140 (1955) 162.
[3] W. Paul, H.P. Reinhard, U. von Zahn, Z. Phys. 152 (1958) 143.
[4] P. Dawson, N. Whetten, Advances in Electronics and Electron Physics, vol. 27, Academic, New York, 1969, 60 pp.
[5] N. McLachan, Theory and Application of Mathieu Functions, Oxford University Press, London, 1951.
[6] P.H. Dawson, Int. J. Mass Spectrom. Ion Phys. 14 (1974) 317.
[7] E.P. Sheretov, V.S. Gurov, M.P. Safonov, I.W. Philippov, Int. J. Mass Spectrom. 189 (1999) 9.
[8] I.E. Dayton, F.C. Shoemaker, R.F. Mozley, Rev. Sci. Instrum. 25 (1954) 485.
[9] D.R. Denison, J. Vac. Sci. Technol. 8 (1971) 266.
[10] A.J. Reuben, A.V. Radchik, G.B. Smith, A.V. Vagov, Rapid Commun. Mass Spectrom. 8 (1994) 939.
[11] A.J. Reuben, G.B. Smith, P. Moses, A.V. Vagov, M.D. Woods, D.B. Gordon, R.W. Munn, Int. J. Mass Spectrom. 154 (1996) 43.
[12] S. Taylor, R.F. Tindall, R.R.A. Syms, J. Vac. Sci. Technol. B 19 (2001) 557.
[13] C.B. Freidhoff, R.M. Young, S. Sriram, T.T. Braggins, T.W. O'Keefe, J.D. Adam, H.C. Nathanson, R.R.A. Syms, T.J. Tate, M.M. Ahmad, S. Taylor, J. Tunstall, J. Vac. Sci. Technol. A 17 (1999) 2300.
[14] J.D. Prestage, NASA Tech. Brief, vol. 23, No. 5; S.M. Colby, J.D. Prestage, PittCon (2000).
[15] S.H. Deshmukh, L.B. King, C.R. Monroe, 40th AIAA/ASME/SAE/ASEE Joint Propulsion Conference and Exhibit, Fort Lauderdale, Florida, July 11–14, 2004.
[16] T. Hayashi, N. Sakudo, Rev. Sci. Instrum. 39 (1968) 958.
[17] T. Hayashi, N. Sakudo, Rev. Sci. Instrum. 40 (1969) 923.
[18] N. Sakudo, T. Hayashi, Rev. Sci. Instrum. 46 (1975) 1060.
[19] G. Bracco, R. Tatarek, S. Terreni, F. Tommasini, U. Linke, J. Electr. Spectrosc. Rel. Phenom. 44 (1987) 197.
[20] A. Pedemonte, R. Gussoni, G. Tatarek, Bracco, Rev. Sci. Instrum. 73 (2002) 4257.
[21] L. Pedemonte, G. Bracco, R. Tatarek, Phys. Rev. A 59 (1999) 3084.
[22] L. Pedemonte, G. Bracco, J. Chem. Phys. 119 (2003) 1433.
[23] G. Bracco, L. Bruschi, R. Tatarek, A. Franchini, V. Bortolani, G. Santoro, Europhys. Lett. 34 (1996) 687.
[24] G. Bracco, D. Cavanna, Phys. Rev. B 76 (2007) 033411.
[25] D.J. Douglas, N.V. Konenkov, Rapid Commun. Mass Spectrom. 16 (2002) 1425.
[26] C. Ding, N.V. Konenkov, D.J. Douglas, Rapid Commun. Mass Spectrom. 17 (2003) 2495.
[27] N. Konenkov, F. Londry, C. Ding, D.J. Douglas, J. Am. Soc. Mass Spectrom. 17 (2006) 1063.
[28] J.R. Gibson, S. Taylor, Rapid Commun. Mass Spectrom. 15 (2001) 1960.
[29] J. Alberty, C. Carstensen, S.A. Funken, Numer. Algor. 20 (1999) 117.
[30] P.-O. Persson, G. Strang, SIAM Rev. 46 (2) (2004) 329.
[31] J. Schulte, P.V. Shevchenko, A.V. Radchikc, Rev. Sci. Instrum. 70 (1999) 3566.
[32] K. Blaum, Ch. Geppert, P. Müller, W. Nörtershäuser, K. Wendt, B.A. Bushaw, Int. J. Mass Spectrom. 202 (2000) 81.
[33] K. Blaum, Ch. Geppert, P. Müller, W. Nörtershäuser, E.W. Otten, A. Schmitt, N. Trautmann, K. Wendt, B.A. Bushaw, Int. J. Mass Spectrom. 181 (1998) 67.
[34] N.V. Konenkov, J.T. Dowell, Int. J. Mass Spectrom. Ion Process. 164 (1997) 201.
[35] J.R. Gibson, S. Taylor, J.H. Leck, J. Vac. Sci. Technol. A 18 (2000) 237.
[36] G. Bracco, M. Canepa, P. Cantini, F. Fossa, L. Mattera, S. Terreni, D. Truffelli, Surf. Sci. 269/270 (1992) 61.
[37] J.R. Gibson, S. Taylor, Rapid Commun. Mass Spectrom. 14 (2000) 1669.
[38] P. Turner, S. Taylor, J.R. Gibson, J. Vac. Sci. Technol. A 23 (2005) 480.
[39] J.R. Gibson, S. Taylor, Rapid Commun. Mass Spectrom. 17 (2003) 1051.